



Development and Testing of Ensemble-Variational Data Assimilation Capabilities for Radar Data within JEDI coupled with FV3-LAM Model

Jun Park¹, Chengsi Liu ¹, Ming Xue^{1,2}

1 Center for Analysis and Prediction of Storms, University of Oklahoma, Norman, Oklahoma, 73072, USA 2 School of Meteorology, University of Oklahoma, Norman, Oklahoma, 73072, USA

Correspondence to: Chengsi Liu (cliu@ou.edu)

Abstract. This study presents the first implementation and evaluation of radar reflectivity data assimilation capabilities within the ensemble three-dimensional variational (En3DVar) data assimilation (DA) system of the Joint Effort for Data assimilation Integration (JEDI) framework. Building on our earlier works that assimilated reflectivity in JEDI LETKF and in GSI En3DVar, this study focuses on the JEDI En3DVar algorithm when coupled with the FV3-LAM model using the Thompson microphysics scheme. The radar reflectivity observation operator is refined by modifying the snow and graupel reflectivity formulations to improve consistency with Thompson microphysics. The new operator notably improves reflectivity analyses at the upper levels and reduces root-mean-square innovations for both reflectivity and radial velocity during the DA cycles. A high-impact convective storm event is used to evaluate the new implementation. DA experiments are conducted using both the JEDI and GSI En3DVar systems, employing identical observation operators and similar configurations. The resulting analyses and short-range forecasts from the two systems are comparable, supporting the validity of the new implementation of JEDI En3DVar for reflectivity and radial velocity assimilation. Additional comparisons with real-time High-Resolution Rapid Refresh (HRRR) and experimental Rapid Refresh Forecast System (RRFS) forecasts are made. The JEDI-based experiment captures the storm structure and placement with accuracy similar to or better than the HRRR and RRFS forecasts. Improvements are especially evident in the depiction of convective cores and stratiform rainbands, where reflectivity intensity and coverage are better aligned with radar observations.

1 Introduction

Accurate prediction of high-impact convective-scale weather events such as supercells, tornadoes, and heavy precipitation remains a critical challenge for both research and operational numerical weather prediction (NWP). High-resolution radar observations, particularly radar reflectivity and radial velocity, offer invaluable information on the internal structure and rapid evolution of convective storms. The assimilation of such radar observations into NWP models has been shown to significantly improve the quality of initial conditions, thereby enhancing short-range forecast skill (e.g., Sun and Crook 1997; Schenkman



30

40

50



et al. 2011; Snook et al. 2012; Sun et al. 2014; Kong et al. 2018; Tong et al. 2020; Labriola et al. 2021; Park et al. 2023; Gao et al. 2024).

Ensemble Kalman filter (EnKF, Evensen 2003) and variational methods are two primary approaches for directly assimilating radar reflectivity. Compared to the variational methods, EnKF is generally easier to implement and provides ensemble of analyses that can be used to initialize ensemble forecasting systems, such as the Global Ensemble Forecast System (GEFS, Zhou et al. 2022) and the High-Resolution Rapid Refresh Ensemble (HRRRE, Kalina et al. 2021) forecasting system of the U.S. National Weather Service (NWS). Both EnKF and variational methods rely on the assumption of Gaussian error statistics. For EnKF, this limitation is particularly evident because the ensemble represents the forecast distribution only through its mean and covariance, making the analyses suboptimal in the presence of strong nonlinearities or non-Gaussian errors, whereas variational methods can partly alleviate such issues through non-quadratic cost functions and variational quality-control schemes (Lorenc 2003). Due to the limited ensemble sizes typically used, EnKF also suffers from rank deficiency with its background error covariance matrix, and ensemble under-dispersion (Houtekamer and Zhang 2016).

Variational methods, including the three-dimensional variational (3DVar), pure or hybrid ensemble-variational (En3DVar) methods, find the analyzed state using by minimizing a variational cost function. The variational framework makes it easier to include both static and ensemble-derived background error covariance in hybrid En3DVar algorithms (Hamill and Snyder 2000; Lorenc 2003). The implementation of variational methods typically requires the development of tangent-linear and adjoint models of observation operators, which increases computational and coding complexity. When the operational operators contain high nonlinearity, such as those of radar reflectivity, difficulties can arise in achieving minimization convergence or even cause instability (Sun and Crook 1997; Liu et al. 2020). The linearization of nonlinear observation operators introduces error; it can be mitigated to some extent by using double-loops, where re-linearization is done in the outer loops around new states obtained in the inner loops, via an effectively iterative procedure (Courtier et al. 1994).

To avoid the use of tangent-linear and adjoint of the nonlinear reflectivity operator, Wang and Wang (2017) introduced a formulation within the GSI-based pure En3DVar system in which radar reflectivity is treated as a state variable. This approach enables the assimilation of reflectivity observations without explicitly involving the reflectivity observation operator in the observation term of the cost function, thereby avoiding the technical complexities associated with operator linearization. With this formulation, the analysis of the hydrometeor variables that otherwise would appear directly within the observation operator rely entirely on ensemble-derived cross-covariances, which may not work well when the ensemble-derived covariance is poorly estimated. Another important issue is that it is not straightforward to include static covariance within hybrid En3DVar algorithm using, e.g., the commonly used extended control variable method (Lorenc 2003).

Several recent studies have focused on improving the direct assimilation of radar reflectivity in variational frameworks, in the areas of solution accuracy and issues related to high nonlinearity of the reflectivity and the consistency of operator with microphysics schemes used. For pure 3DVar without the help of reliable cross-covariances, Liu et al. (2019) introduced temperature-dependent background error profiles for hydrometeor variables to enable physically realistic partitioning between liquid and ice hydrometeors. Liu et al. (2020) identified minimization convergence issues related to the



75



use of hydrometeor mixing ratios as control variables and proposed two treatments: applying a lower bound on reflectivity to avoid instability with cost function gradient calculations; and employ separate variational analysis passes for radial velocity and reflectivity data to avoid the dominance of the reflectivity observation term in the cost function. These treatments significantly improved analysis stability and accuracy.

Chen et al. (2021) introduced power-transform to the hydrometeor control variables, allowing for the adjustment to the nonlinearity of the control variable and observational variable relationship through a tunable exponent of the power transform. Their results showed much faster and more effective cost function convergence and reduced spurious analysis increments. Building upon this, Li et al. (2022) further applied a similar power transform to the total number concentration of rainwater associated with a double-moment microphysics used in the prediction model which further improved the analysis. In Liu et al. (2022), the reflectivity observation operator was reformulated to be consistent with the Thompson microphysics scheme (Thompson et al. 2008) used. The operator and its adjoint were implemented in the En3DVar system within the Gridpoint Statistical Interpolation (GSI, Kleist et al. 2009) framework, and the new operator led to improved analyses and short-range forecasts compared to those using single-moment-based operators.

Three methods for assimilating radar reflectivity have been developed and implemented in GSI: indirect assimilation through cloud analysis (e.g., Banos et al. 2022; Dowell et al. 2022), used operationally in the High-Resolution Rapid Refresh (HRRR) system (Benjamin et al. 2016); direct method based on the reflectivity-state-variable approach (Wang and Wang 2017), which has been adopted in the initial version of the Rapid Refresh Forecast System (RRFSv1, Banos et al. 2022; Carley et al. 2023); and a traditional variational approach that includes the reflectivity observation operator along with its tangent-linear and adjoint components in the cost function, which are formulated to be consistent with model microphysics (Liu et al. 2022).

The Joint Effort for Data assimilation Integration (JEDI; Trémolet and Auligné 2020) is being developed as the next-generation DA system for NOAA's Unified Forecast System (UFS), with the goal of replacing the current GSI framework. JEDI is designed to be modular, extensible, and model-agnostic, enabling community-driven development and supporting both research and operational applications across coupled Earth system components. Recent progress has demonstrated the feasibility of assimilating radar observations within JEDI using variants of the EnKF method. Park et al. (2023) implemented radar DA in JEDI coupled with the FV3-LAM model (Lin 2004) using the Local Ensemble Transform Kalman Filter (LETKF, Hunt et al. 2007) and the gain-form localization version of LETKF (LGETKF, Bishop et al. 2017), showing promising results in the analysis and short-range prediction of convective storms. However, Park et al. (2023) was limited to demonstrating reflectivity and radial velocity assimilation using the LETKF and LGETKF ensemble algorithms in JEDI. In contrast, the assimilation with En3DVar requires the implementation and testing of tangent-linear and adjoint components, which are highly desirable within JEDI. In fact, the core of the data assimilation systems in current NWS operational regional forecasting models is the hybrid En3DVar, although it is based on the GSI framework (Hu et al. 2017; Wu et al. 2017; Dowell et al. 2022). Therefore, the development of direct reflectivity assimilation capabilities within the JEDI variational framework is both



105

110

120



desirable and timely. This work addresses this gap by developing and implementing the tangent-linear and adjoint of the reflectivity operator in the JEDI variational system, enabling variational assimilation of radar reflectivity.

Specifically, this study refines a radar reflectivity observation operator to improve its consistency with the double-moment Thompson microphysics scheme, which is used in the current operational HRRR and the next-generation RRFS. The refined operator is implemented in both the GSI and JEDI En3DVar systems, thereby enabling direct variational assimilation of reflectivity within JEDI. A convective storm case is then used to test and evaluate the new operator, with forecasts compared against those of the operational HRRR, which still employs indirect cloud analysis, and an experimental RRFS that uses the reflectivity-state-variable approach. The evaluation highlights the impacts of the refined operator on the analysis and short-range prediction of convective precipitation and storm structure.

The remainder of this paper is organized as follows. Section 2 describes the refinement of the reflectivity observation operator. Section 3 introduces the test case, and presents the forecast model and DA configurations, and the design of the DA experiments. Section 4 presents the results, including the evaluations of the refined operator, intercomparisons between the JEDI and GSI systems, and baseline forecast comparisons against independent operational HRRR and RRFS prototype runs from the 2022 Hazardous Weather Testbed Spring Forecast Experiment (NOAA 2022). Section 5 summarizes the key findings and discusses their implications, along with potential directions for future work.

2 Reflectivity observation operator for Thompson microphysics

The radar reflectivity Z is defined as

$$Z = 10 \log_{10} Z_e \,, \tag{1}$$

where Z_e is the equivalent reflectivity factor that contains contributions from various hydrometeor species. Thompson microphysics scheme employs a double-moment formulation for rainwater that predicts the mixing ratios and total number concentrations. Therefore, Z_e is computed from the mixing ratios of precipitating hydrometeors of rainwater (q_r) , snow (q_s) , and graupel (q_g) , along with the total number concentration of rainwater (N_t) , according to

$$Z_e = Z_{er}(q_r, N_{tr}) + Z_{es}(q_s) + Z_{eg}(q_g).$$
 (2)

The rainwater contribution to the equivalent reflectivity, Z_{er} , is computed from the mixing ratio q_r and the total number concentration N_{tr} , which are explicitly predicted. Assuming spherical raindrops and using the Rayleigh scattering approximation, Z_{er} is calculated as

$$Z_{er} = \frac{10^{18} \times 720(\rho q_r)^2}{\pi^2 \rho_r^2 N_{tr}},\tag{3}$$

where ρ is the air density, and ρ_r is the density of rainwater.

In the Thompson microphysics, the snow particle size distribution is represented as a sum of an exponential and a gamma distribution, with parameters that depend on temperature and snow mixing ratio (Thompson et al. 2008). For graupel,



135

145



the intercept parameter varies with graupel mixing ratio and temperature, and distinct densities are assumed above and below 0 °C (dry/wet states). These scheme-specific details yield piecewise and state-dependent formulations in WRF that are not well suited for constructing smooth, differentiable tangent-linear and adjoint operators required by En3DVar. Therefore, where closed-form mappings exist (e.g., rain and dry snow) we apply them directly, and for wet snow and temperature-dependent graupel we use compact least-squares power-law relations fit to reflectivity diagnosed from the Thompson scheme. This approach preserves consistency with microphysics while providing the smooth derivatives needed for stable variational minimization.

In this study, the contributions of snow and graupel to reflectivity are treated differently than in Liu et al. (2022), which employed power-law approximations to the model-predicted mixing ratios using fitted curves directly derived from Thompson microphysics output. While parameterized relationships are still used here, a key improvement of the updated operator is the explicit incorporation of temperature-dependent melting effects, which distinguish between wet and dry states of hydrometeors by applying separate formulations above and below the freezing level.

For snow, reflectivity calculations are separated into wet and dry snow conditions based on air temperature. For the wet snow state (air temperature T>0°C), we developed a simplified power-law function based on the snow mixing ratio q_s , expressed as

$$Z_{es} = a_{wet}(\rho q_s)^{b_{wet}},\tag{4}$$

where ρ is the air density, and the empirically derived coefficients are $a_{wet} = 1.47 \times 10^5$ and $b_{wet} = 2.67$. These values were obtained by curve fitting to simulated reflectivity data from the Thompson microphysics scheme under wet snow conditions.

For the dry snow state (air temperature $T \le 0$ °C), the radar reflectivity factor is computed following Thompson et al. (2008) and Field et al. (2005). It is given by

$$Z_{es} = C_{dry}a(T)(\rho q_s)^{b(T)}, \tag{5}$$

and constant C_{dry} is defined as

$$C_{dry} = \left(\frac{0.176}{0.93}\right) \left(\frac{6}{\pi}\right)^2 \left(\frac{0.069}{900}\right)^2 = 4.06 \times 10^{-9}.$$
 (6)

For graupel, the equivalent reflectivity factor Z_{eg} is also separated into two regimes depending on air temperature. Following the Thompson microphysics scheme, different graupel densities are assumed for temperatures above and below freezing. Accordingly, we apply two separate expressions for Z_{eg} :

$$Z_{eg} = \begin{cases} \frac{10^{15.25} \times 720 \rho^{1.75} q_g^{2.5}}{\pi^{1.75} \rho_g^{1.85}} & T > 0 \text{ °C,} \\ \\ \frac{10^{16.5} \times 720 \rho^{1.75} q_g^{2.5}}{\pi^{1.75} \rho_g^{2.3}} & T \leq 0 \text{ °C.} \end{cases}$$
(7)

where ρ_q is the graupel density.



165

170



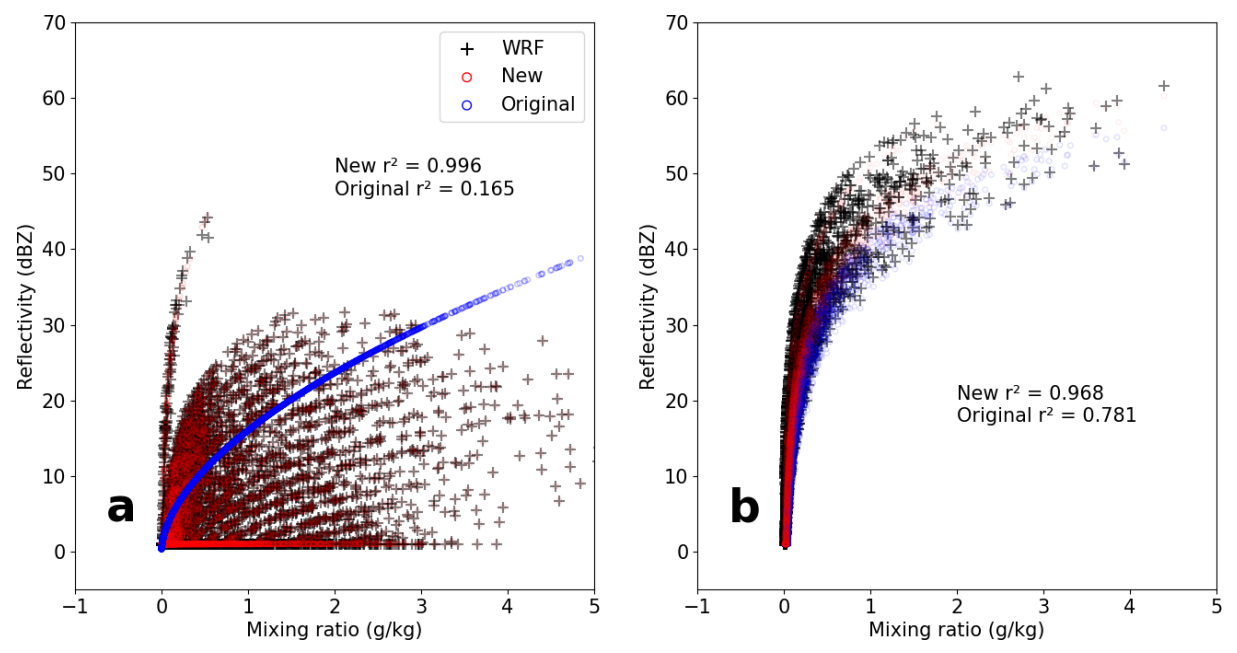


Figure 1. Scatterplots comparing the fitted relationships between radar reflectivity (dBZ) and mixing ratio (g kg⁻¹) for (a) snow and (b) graupel predicted using the Thompson microphysics scheme. Black dots show reflectivity values diagnosed directly from WRF model output. The red and blue circles indicate reflectivity computed using the updated and original observation operators, respectively. Coefficients of determination (r2) measure the agreement between each operator and the WRF-diagnosed reflectivity.

To evaluate the operator consistency with the Thompson microphysics, reflectivity from the updated operator and the original operator of Liu et al. (2022) is compared with values diagnosed directly from the WRF model (Fig. 1). For snow, the Thompson scheme represents the PSD as the sum of an exponential and a gamma distribution with parameters that depend on temperature and snow content, which naturally produces a broad spread of WRF-diagnosed reflectivity at a given mixing ratio. The updated operator introduces separate temperature-dependent relations for wet and dry snow; the wet-snow branch on the left side of Fig. 1a closely follows the model-diagnosed values, raising the agreement to $r^2 = 0.996$ (versus 0.165 for the original). For graupel, the intercept parameter varies with mixing ratio and temperature, and different densities are assumed above and below 0 °C; these state dependencies likewise broaden the diagnosed spread. By explicitly accounting for the temperature dependence and density regimes, the updated graupel relation improves the agreement to $r^2 = 0.968$ (versus 0.781 for the original). the updated relations provide a compact power-law approximation to the Thompson scheme, retaining its key dependencies while ensuring smooth derivatives required by the tangent-linear and adjoint operators.

3 Test case and experiment setup



185



175 3.1 Case overview

Figure 2 shows the observed composite reflectivity from the Multi-Radar Multi-Sensor (MRMS, Smith et al. 2016) at 0000 UTC 13 May 2022, a well-organized, north—south-oriented convective line with a pronounced bowing segment over the Upper Midwest. A negatively tilted upper-level trough over the Midwest, combined with a low-level jet under an omega block pattern, facilitated northward transport of moisture and instability. A surface low formed over the western Midwest with an associated southward-extending cold front and a warm front located in Minnesota.

Severe weather events and observations were reported across the midwestern contiguous United States (CONUS) within the verification domain (black box in Fig. 2). For example, at 2125 UTC 12 May, a Road Weather Information System weather station in Hutchinson County, South Dakota, recorded a wind gust of 107 mph. Additionally, six tornadoes in South Dakota and four in Minnesota were reported between 2300 UTC 12 May and 0000 UTC 13 May. Between 0000 and 0200 UTC 13 May 2022, the primary forecast period of interest in this study, 17 tornadoes and 128 severe wind reports were observed across the north-central CONUS and the Great Plains, according to reports from the Storm Prediction Center.

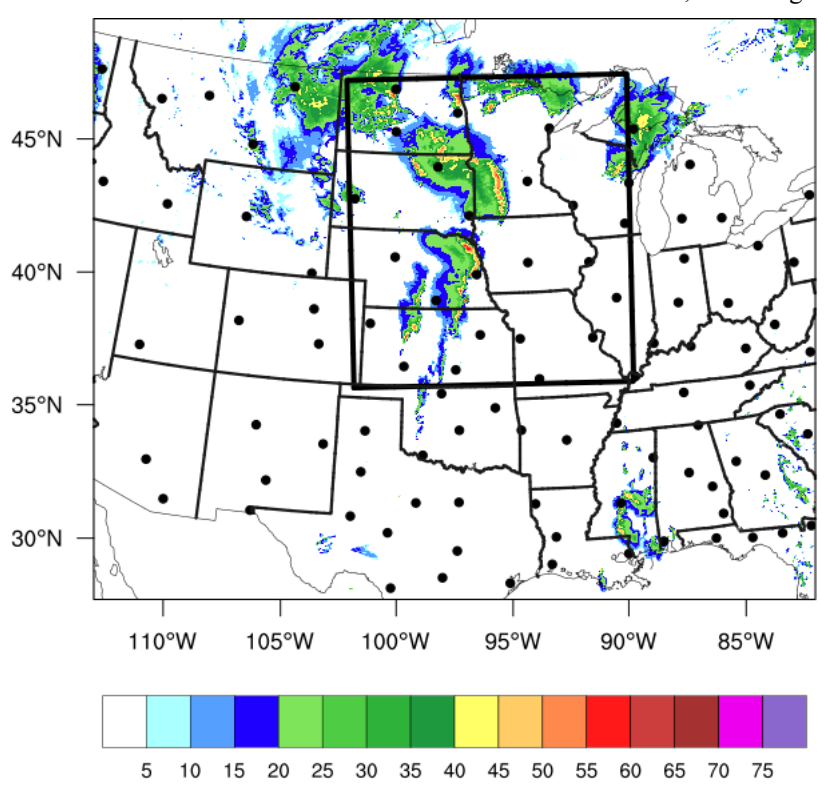


Figure 2. MRMS composite reflectivity (dBZ) at 0000 UTC 13 May 2022. The bold black box marks the verification domain, and WSR-88D radar locations are indicated by black dots.





190 3.2 Experiment setup

3.2.1 Model configuration

The numerical experiments utilize the FV3-LAM configured with the RRFS_v1beta physics suite from the Common Community Physics Package (CCPP, Bernardet et al. 2024). The physics parameterizations include the Thompson microphysics scheme (Thompson et al. 2008) without aerosol coupling, the Mellor-Yamada-Nakanishi-Niino (MYNN) planetary boundary layer (PBL) scheme (Olson et al. 2019), the Rapid Radiative Transfer Model for GCMs (RRTMG) radiation scheme (Iacono et al. 2008), and the Noah-MP land surface model (Niu et al. 2011). The computational domain covers the midwestern United States, spanning 1050×850 horizontal grid points on an extended Schmidt projection grid at approximately 3-km horizontal grid spacing (Fig. 1). In the vertical, a terrain-following hybrid sigma-pressure coordinate with 66 vertical levels is employed, with the model top is located near 214 hPa, consistent with RRFS v1beta.

3.2.2 Data assimilation system

The radar DA experiments are conducted using En3DVar algorithms implemented within the GSI and JEDI frameworks. In both systems, ensemble perturbations for constructing flow-dependent background error covariances in En3DVar are generated using a variant of EnKF: the ensemble square root filter (EnSRF; Whitaker and Hamill 2002) in GSI and the LETKF (Hunt et al. 2007) in JEDI. These ensemble DA cycles are run in parallel with the En3DVar systems, and ensemble forecasts initialized from ensemble analyses in each cycle provide ensemble perturbations for En3DVar. Relaxation to prior spread (RTPS; Whitaker and Hamill 2012) ensemble inflation is applied with a coefficient of 0.99 to help maintain the ensemble spread. Ensemble localization is performed using a recursive filter in GSI En3DVar (Purser et al. 2003) and Background error on an Unstructured Mesh Package (BUMP; Ménétrier 2020) in JEDI, with horizontal and vertical localization scales of 18 km and 0.7 ln(P), respectively.

As part of this study, the radar reflectivity observation operator previously implemented within for GSI (Liu et al. 2022) is first migrated into the Unified Forward Operator (UFO) module of JEDI. This operator follows the formulations introduced in section 2 and includes both forward operators and their tangent linear and adjoint components. The implementation enables variational assimilation of reflectivity in JEDI, and these capabilities have been publicly released as part of the JEDI community codebase after testing described in this paper as well as additional testing were completed. The analysis variables updated by the DA include zonal wind (u), meridional wind (v), air temperature (T), specific humidity (q_v) , layer pressure thickness (delp), rainwater (q_r) , snow (q_s) , graupel (q_g) , cloud water (ql), cloud ice (qi), and number concentration of rainwater (q_{nr}) . To address nonlinearity in the reflectivity observation operator, power-transformed control variables are adopted for hydrometeor fields following Chen et al. (2021) and Li et al. (2022).

220

215

200

205



225



3.2.3 Radar observations

Radar reflectivity (Z) and radial velocity (Vr) observations are assimilated within a ± 3 -minute window around each analysis time. Reflectivity data are prepared from the MRMS mosaic, and radial velocity data from 40 operational WSR-88D radars are used, after automated quality control processes that include noise removal, clutter suppression, despeckling, and velocity dealiasing (Brewster et al. 2005). Observation errors are assumed constant at 5 dBZ for reflectivity and 3 m s⁻¹ for radial velocity. Reflectivity in clear-air regions in the MRMS data are set to 0 dBZ during assimilation, and radial velocity observations are used only where observed reflectivity exceeds 5 dBZ.

3.2.4 Experiment design

The DA experiments consist of a 1-hour model spin-up followed by five hourly assimilation cycles between 1900 UTC 12 May and 0000 UTC 13 May 2022 (Fig. 3). The initial ensemble is generated from a 30-member GEFS analysis ensemble initialized at 1800 UTC 12 May. Each member is integrated forward using FV3-LAM for one hour to provide the initial background for the first assimilation cycle. Lateral boundary conditions are taken from 3-hourly GEFS ensemble forecasts initialized 1800 UTC 12 May.

Four experiments are conducted: (1) NODA, a baseline run without radar data assimilation; (2) GSI-New, which uses EnSRF-updated ensembles and a modified reflectivity operator in GSI En3DVar; (3) JEDI-Org, which uses LETKF-updated ensembles and the original reflectivity operator in JEDI En3DVar; and (4) JEDI-New, which is similar to JEDI-Org but uses the modified reflectivity operator. In all En3DVar experiments, no static background error covariance is included; thus, the algorithms are pure En3DVar rather than hybrid. For baseline comparison, forecasts from HRRR and RRFS prototype 2 during the 2022 HWT Spring Forecast Experiment are also included. All experiments produce 6-hour ensemble forecasts initialized from the final analyses at 0000 UTC 13 May.





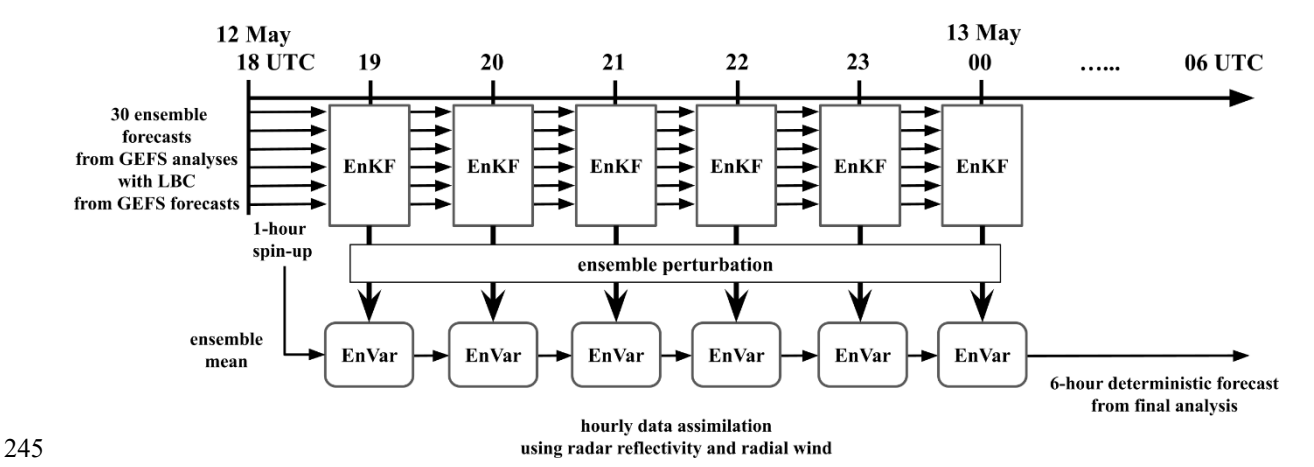


Figure 3. Flow diagram of the radar data assimilation experiment. A 1-hour model spin-up from GEFS ensemble initial conditions is followed by five hourly assimilation cycles between 1900 UTC 12 May and 0000 UTC 13 May 2022. Final analyses are used to launch 6-hour ensemble forecasts.

4 Results and discussions

250

255

260

265

4.1 Impact of radar data assimilation on En3DVar analyses

Figure 4 shows the root-mean-square innovation (RMSI) and mean innovation diagnostics for assimilated radar reflectivity and radial velocity during DA cycles. Compared to the NODA baseline, all radar assimilation experiments significantly reduce RMSIs for both Z and Vr (Figs. 4a, c), with steady decreases in Z RMSI throughout the assimilation period (Fig. 4a). Notably, JEDI-New consistently show improved performance over JEDI-Org, resulting in a lower RMSI of approximately 1.5 dBZ in the background and 3 dBZ in the analysis at the final cycle (Figs. 4a, b). This reduction highlights the impact of the updated reflectivity observation operator in JEDI. Mean innovations further confirm this improvement. The large positive reflectivity biases seen in the NODA experiment are substantially reduced in all radar-assimilation experiments. JEDI-New consistently outperforms JEDI-Org, especially in the background forecasts of reflectivity (Figs. 4e, f).

For Vr, all DA experiments reduce the background RMSI relative to NODA (Fig. 4c), and their analysis RMSIs remain around 2.0 m s⁻¹ (Fig. 4d). However, JEDI-Org exhibits slightly higher RMSIs and mean innovations than JEDI-New and GSI-New (Figs. 4d and 4h), and difference is the largest in the V_r analyses between JEDI-New and JEDI-Org (Fig. 4d). This result suggests that inaccuracies in the reflectivity analysis associated with the use of a less accurate observation operator can lead to degraded wind analyses through multivariate correlations in the variational update. Notably, JEDI-New and GSI-New produce nearly identical diagnostics throughout the assimilation period, despite differences in the ensemble DA methods and assimilation frameworks. These results indicate that JEDI-New can match the performance of GSI En3DVar when the same improved reflectivity observation operator is used. Since the reflectivity assimilation capabilities in GSI had been tested and reported in previous papers (Chen et al. 2021; Li et al. 2022; Liu et al. 2022), the comparison serves to demonstrate the validity of our implementation within JEDI.





275

280

285

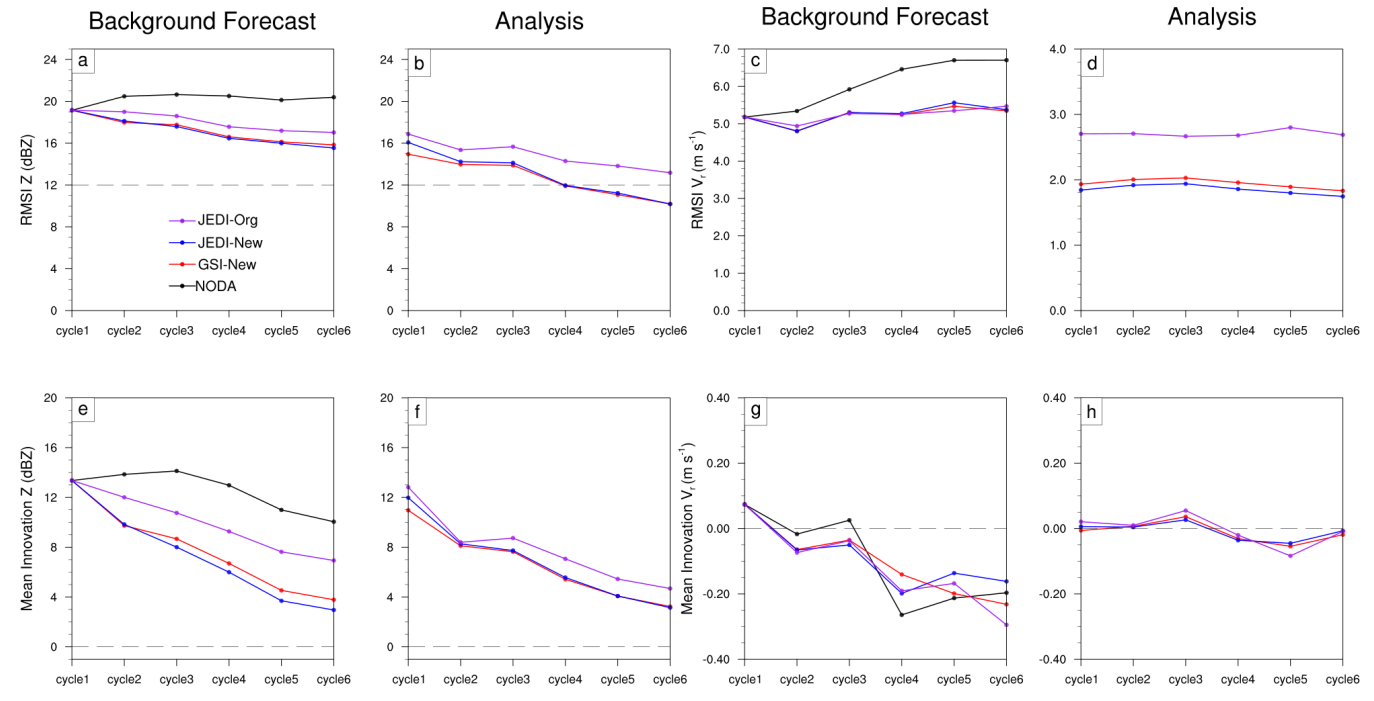


Figure 4. The observation-space diagnostics from the backgrounds and analyses for the assimilated reflectivity and radial wind observations. For the Z diagnostics, they are calculated when observed Z or calculated H(x) is greater than or equal to 15 dBZ.

Figure 5 compares composite reflectivity fields at the final analysis time (00 UTC 13 May 2022) among different DA experiments with the MRMS observations. The MRMS field (Fig. 5a) features a well-organized convective system across the Upper Midwest, including a north-south-oriented convective line with a bowing structure in the north and a localized curved reflectivity feature in the south. Without radar DA, the NODA (Fig. 5e) fails to capture the key storm structures. It misses the echo coverage in western Minnesota and along the South and North Dakota border and displays weak, poorly organized convection that significantly deviates from the observed reflectivity pattern.

In contrast, the DA experiments substantially improve the representation of the convective system. The benefits of the updated reflectivity operator are clearly evident in the background fields. Compared to JEDI-Org (Fig. 5c), JEDI-New (Fig. 5d) produces stronger and better-placed reflectivity along the leading convective line and shows broader coverage in the post-line region. JEDI-Org underrepresents the trailing stratiform or weak echo region behind the convective line, resulting in a less complete depiction of the convective system. The JEDI-New background structure more closely resembles that of GSI-New (Fig. 5b), which also captures both the leading convective band and the accompanying trailing echoes. These comparisons demonstrate the ability of the updated Z operator to improve short-term forecast fields.

In the analysis fields, both GSI-New (Fig. 5f) and JEDI-New (Fig. 5h) produce well-organized convective structures that closely resemble the MRMS observation, successfully capturing the bowing segment in the north and the hook echo





structure in the south. In contrast, the JEDI-Org analysis (Fig. 5g) shows less coherent storm organization, particularly in the southern segment, where the hook echo is poorly represented.

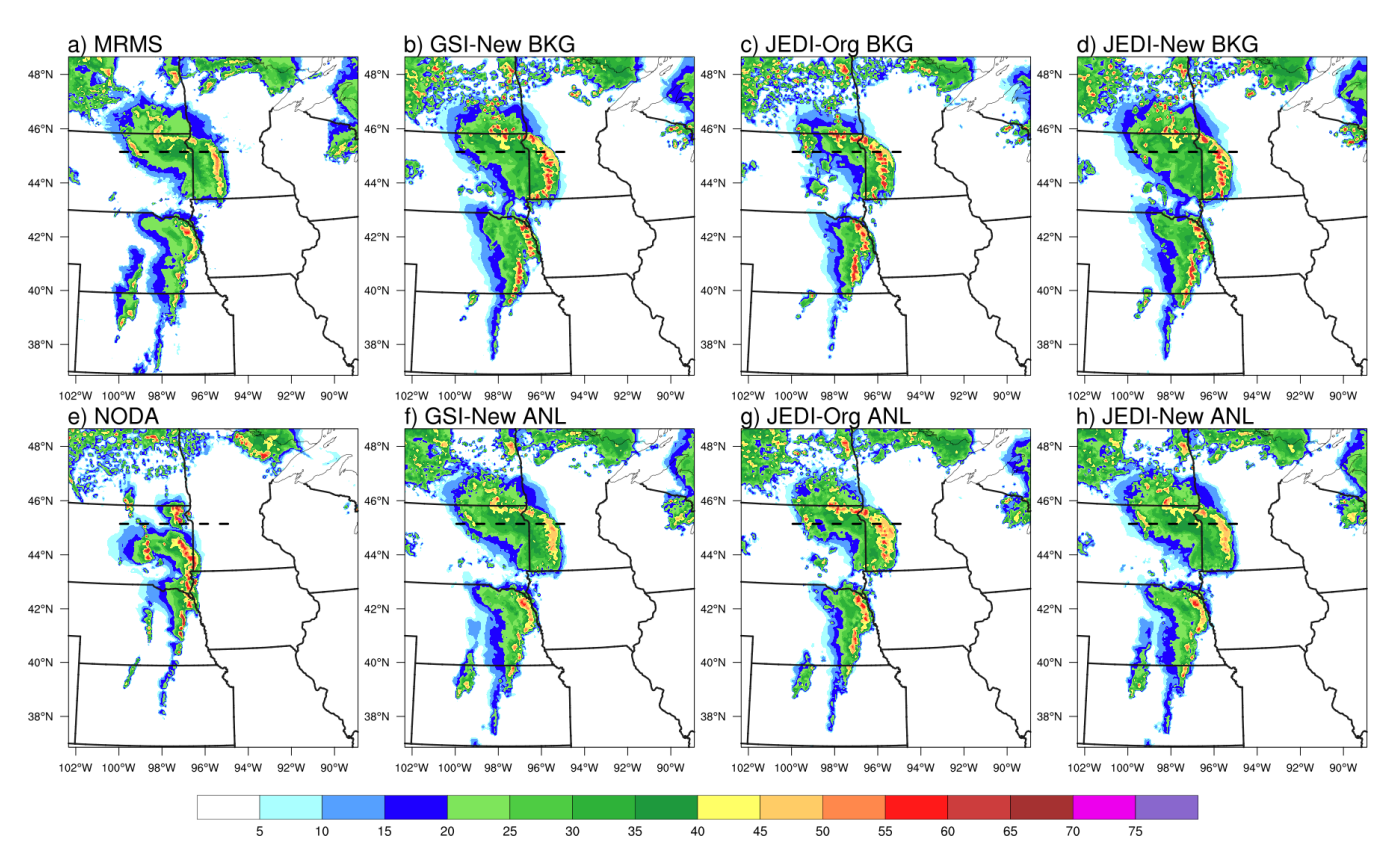


Figure 5. The composite reflectivity at final analysis time (00 UTC on May 13, 2022) from the observation and observation-space diagnostics from background forecasts and the analyses of the NODA, GSI En3DVar and JEDI En3DVar experiments using the original and modified Z observation operators. The dashed lines inside the panels show the locations of vertical cross sections shown in Figs. 6 and 7.

Figure 6 shows vertical cross sections of composite reflectivity at the final analysis time (00 UTC 13 May 2022) along the dashed line in Figure 5. The MRMS observation (Fig. 6a) displays a well-developed deep convective system, featuring two upright convective towers: a dominant one near 95°W and a secondary one near 96.5–97°W. Both towers exhibit echo tops exceeding 14 km and strong reflectivity cores (≥50 dBZ) through the mid-levels. In contrast, the NODA analysis (Fig. 6e), which does not assimilate radar observations, exhibits a notable northward displacement of the convective system relative to the MRMS analysis. As a result, the main convective core is located outside the cross-section domain shown in Fig. 5e, leading to the apparent absence of deep echoes in the vertical structure.

In the background fields, all DA experiments reproduce the main convective tower near 95°W but overestimate its midlevel reflectivity intensity. This bias is most evident in JEDI-New (Fig. 6d), where reflectivity exceeds 60 dBZ between 5–8 km, stronger than both GSI (Fig. 6b) and JEDI-Org (Fig. 6c). These overamplified cores are likely related to excessive graupel reflectivity associated with the Thompson microphysics scheme, consistent with findings in Liu et al. (2022) and Grim

295



320



et al. (2023). Additionally, none of the background fields capture the western secondary tower near 96.5–97°W, which is prominent in the observation.

The analysis fields show that radar DA successfully recovers this missing western feature. JEDI-New (Fig. 6h) reconstructs the secondary convective tower with reflectivity intensity and echo-top height comparable to MRMS, whereas GSI (Fig. 6f) and JEDI-Org (Fig. 6g) underestimate its strength and vertical extent. In the primary tower region near 95°W, JEDI-New also effectively reduces the midlevel overestimation seen in the background. By contrast, JEDI-Org retains an overly strong midlevel core and exhibits limited vertical development.

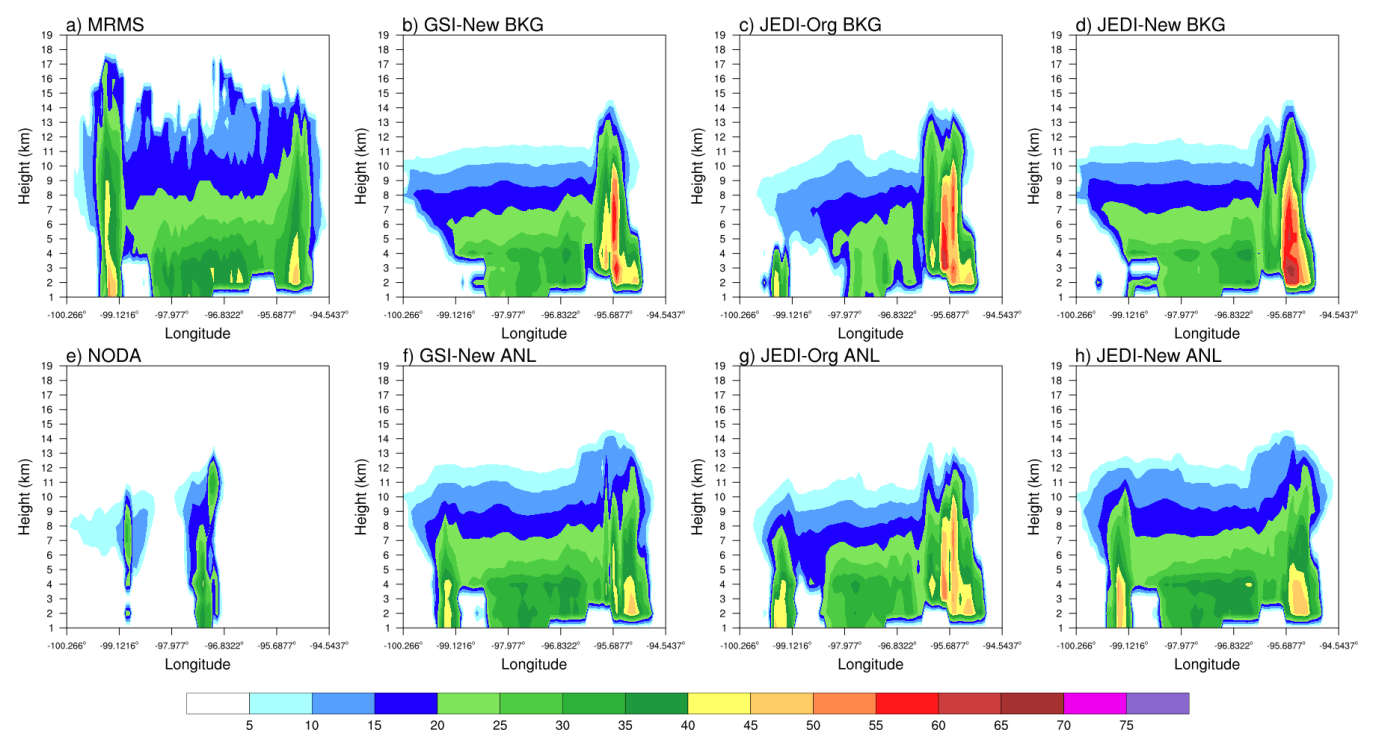


Figure 6. Vertical cross sections of composite reflectivity at the final analysis time (00 UTC 13 May 2022) along the dashed line shown in Fig. 5, from the MRMS observation, and the background and analysis fields of the NODA, GSI-New, JEDI-Org, and JEDI-New experiments.

To further understand the reflectivity differences noted in Fig. 6, we examine vertical cross sections of the analysis increments for rainwater, snow, and graupel mixing ratios shown in Fig. 7. Since radar reflectivity is a nonlinear function of multiple hydrometeor species, differences in its assimilation impacts can help explain the variations in analyzed reflectivity structures.

Among the three hydrometeor species, snow shows the most prominent differences between JEDI-New and JEDI-Org. In the snow analysis increments (Figs. 7b, e, h), JEDI-Org (Fig. 7b) exhibits weak and spatially fragmented increments, suggesting minimal adjustments to the snow field. In contrast, JEDI-New (Fig. 7e) produces broad and coherent positive snow increments in the mid- to upper levels (model levels ~15–45), especially over the main convective towers. The magnitude and



330

335

340



coverage of these increments are comparable to those from GSI En3DVar (which uses the updated Z operator) (Fig. 7h), indicating that the updated reflectivity operator in JEDI-New enables more effective retrieval and correction of snow content, which contributes significantly to the improved vertical structure of reflectivity shown in Figure 6.

For graupel (Figs. 7c, f, i), JEDI-Org again shows little impact from radar DA, with only weak and localized adjustments. In contrast, JEDI-New (Fig. 7f) and GSI (Fig. 7i) both exhibit pronounced negative increments centered around the mid-levels of the primary convective tower. This indicates a reduction in excessive background graupel, which likely contributes to the overly strong midlevel reflectivity in the background field. In contrast, the rainwater increments (Figs. 7a, d, g) are relatively weak and similar across all experiments, reflecting the fact that the treatment of rainwater is unchanged between the original and updated operators. Thus, differences among experiments arise mainly from the handling of snow and graupel rather than from rainwater.

These results confirm that the improved reflectivity analysis in JEDI-New is primarily associated with the refined representation and updating of the snow and graupel fields. The updated Z observation operator ensures greater consistency with the Thompson microphysics scheme, particularly in the treatment of frozen hydrometeors, leading to analyses that better align with model-computed reflectivity fields and more accurate reconstructions of convective vertical structures. For the rest of this paper, we will focus on the evaluation of DA experiments using the new Z operator, i.e., the GSI-new and JEDI-new experiments.





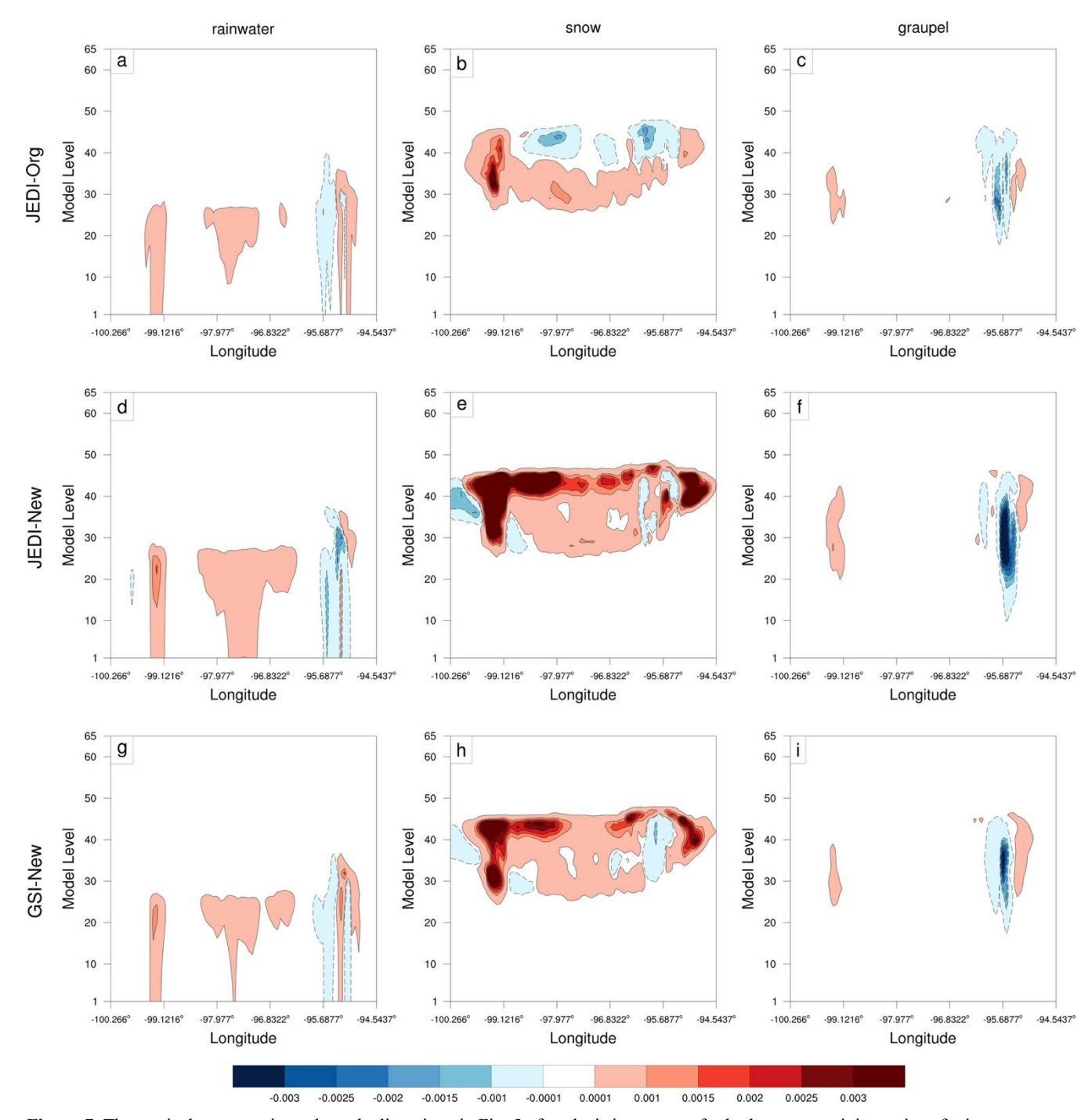


Figure 7. The vertical cross sections along the line given in Fig. 5 of analysis increments for hydrometeor mixing ratios of rainwater, snow, and graupel at final analysis time (00 UTC on May 13, 2022) from GSI En3DVar and two JEDI En3DVar experiments.



350

355

360

365

370



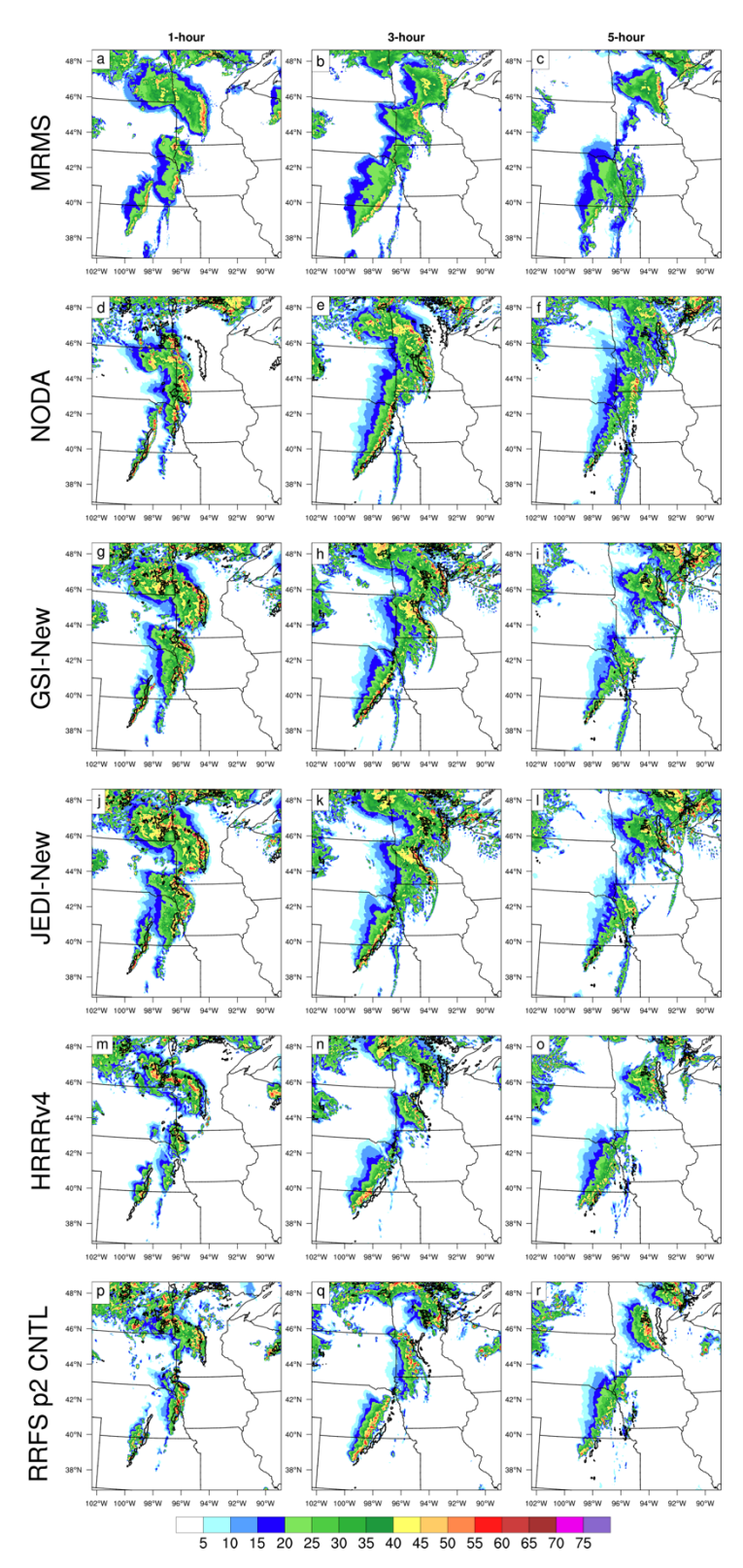
4.2 Impacts on forecasts

For qualitative assessment of forecast performance, the forecasts initialized from the final En3DVar analyses from GSI-new and JEDI-new are compared with those from the no-DA baseline experiment (NODA), and two reference forecasts representative of the current and potential future operational configurations, i.e., the HRRR version 4 (HRRRv4) and the RRFS prototype 2 control run (RRFSp2 CNTL). As shown in Fig. 8, NODA experiment fails to reproduce key convective features observed in the MRMS composite reflectivity. In the 1-h forecast, it entirely misses the convective line over Minnesota and instead produces a broad, unrealistically merged system (Fig. 8d). The forecast also exhibits notable displacement of the bow echo structures across central CONUS throughout the 3 and 5 hours of forecast (Figs. 8e–f). In contrast, both the GSI and JEDI En3DVar DA experiments successfully capture the convective line in Minnesota at 1 h (Figs. 8g, j) and reproduce a trailing stratiform precipitation region behind the leading convective line. At later lead times, the En3DVar experiments maintain a better alignment of high-reflectivity structures over Kansas and Nebraska (Figs. 8h–i, k–l), although some degradation in intensity and coverage is evident compared to the 1-h forecasts.

The two reference forecasts, HRRRv4 and RRFS p2 CNTL, also capture the general structure of the observed convective systems, particularly the split into northern and southern convective segments. However, positional and structural differences are apparent upon closer inspection. The HRRRv4 forecast shows a weaker bow echo and a southeastward displacement of the Minnesota line as early as 1 h (Fig. 8m), with this error persisting through 5 h. Compared to HRRRv4, RRFS p2 CNTL better captures the structure of the northern convective line at 1 h, but tends to underpredict reflectivity intensity and spatial extent, especially in the southern segment at longer lead times. Additionally, both reference forecasts display smaller overall high-reflectivity coverage relative to those of En3DVar experiments. This difference is likely attributable to the use of cloud analysis for radar DA in HRRRv4 and the Z-state-variable approach in RRFS p2 CNTL, both of which differ from the direct reflectivity assimilation employed in the En3DVar experiments here. Nonetheless, spurious echo generation is also evident in the En3DVar runs at later lead times, particularly over the northern and northeastern domain area (Figs. 8f, i, l), which may be related to the lack of other data sources in our DA experiments, i.e., only radar data are assimilated. These differences may also reflect intrinsic model characteristics; composite reflectivity forecasts from FV3-LAM tend to be stronger than those from HRRRv4, which is based on the WRF model, consistent with findings in Grim et al. (2023). Overall, the results shows the benefits of directly assimilating reflectivity and radial velocity, in capturing key convective structures in the analysis and forecast, while also highlighting certain sensitivities to model and assimilation methodologies.









380

385

390

395



Figure 8. Composite reflectivity at 1 h (left column), 3 h (middle column) and 5 h (right column) from MRMS observation (first row), and forecasts from NODA, GSI-New, JEDI-New experiments, and from HRRRv4, and RRFSp2 CNTL as labeled. Observed composite reflectivity of 40 dBZ is contoured in black in the forecasts.

Although radar reflectivity assimilation primarily constrains hydrometeor fields, the maintenance and evolution of convective systems also depend on adjustments to thermodynamic and kinematic variables such as temperature, water vapor, pressure, and wind. Since 2-m equivalent potential temperature θ_e and 10-m wind fields are only indirectly impacted by radar DA (via the cross covariances), the fields are partly the results of model response to other more directly impacted fields, through the DA cycles. We examine these fields in the final analyses to see if the DA is producing physically consistent near-surface analyses, in particular in the presentation of the cold pools.

Figure 9 shows 2-m θ_e and 10-m wind fields from UnRestricted Mesoscale Analysis (URMA, NOAA 2018) and the final analyses from the NODA and GSI and JEDI En3DVar DA experiments. Compared to URMA (Fig. 9a), NODA (Fig. 9b) produces cold pools that much smaller in extent than URMA, and the leading edge of the cold pool or the guest front stays close to the South Dakota–Minnesota border while those is URMA and the two DA experiments are much closer in cold pool extents and gust front positions (Fig. 9a,c,d). There are consistent strong surface winds in the cold pool immediately behind the gust front, and the cold pool structure is also consistent with the observed 30 dBZ reflectivity contours, with strong surface divergences underneath and immediately behind the strong echoes. (Figs. 9c and 9d).

Further south and east of the gust fronts, over Kansas, Missouri and Iowa, the DA experiments also show improved inflow structures (Figs. 9c, d), with stronger southerly winds that are more consistent with URMA than NODA (Fig. 9b). The improved analyses of near surface fields indicate that the radar DA can indirectly improve surface temperature, moisture, and wind fields by leveraging cross-variable covariances derived from the ensemble. The apparent too low θ_e in northwest Nebraska and southern South Dakota in both NODA and the DA experiments is likely due to too strong evaporative cooling within the model, which is sensitive to the microphysics scheme used (e.g., Dawson et al. 2010). The assimilation of additional surface observations may be able to improve it somewhat (e.g., Schenkman et al. 2011).





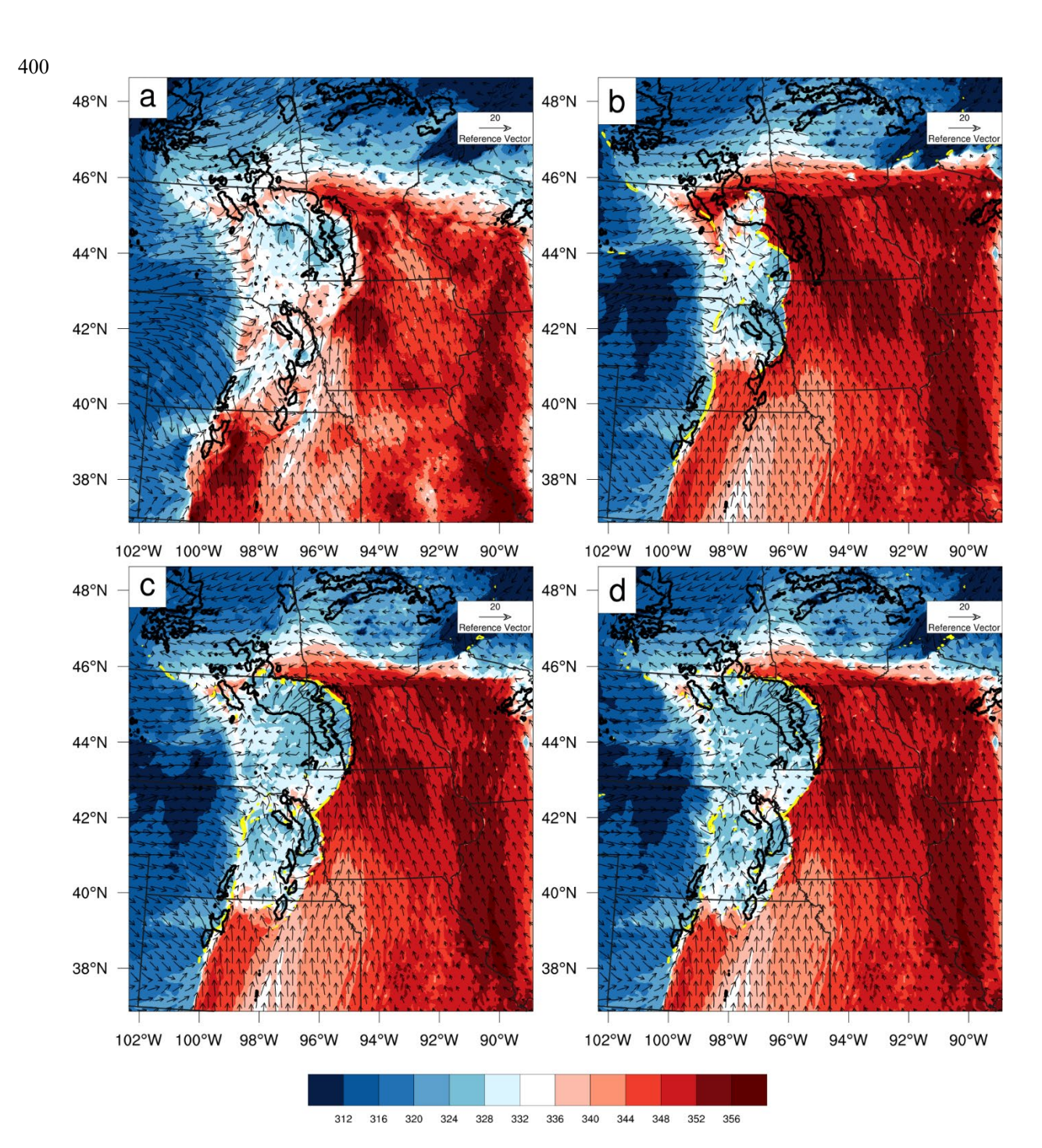


Figure 9. Equivalent Potential Temperature (Shaded; K) at 2 m and wind vectors at 10 m (m s-1) for a) URMA, (b) NODA, (c) GSI En3DVar, and (d) JEDI En3DVar. Black contours in plots denote the areas of observed composite reflectivity exceeding 30 dBZ threshold. Yellow contours show relative vorticity exceeding 100×10^{-5} s⁻¹ from model level 1 (lowest model level)



410

415

425



Figure 10 presents the fractions skill scores (FSS; Roberts and Lean 2008) of forecast composite reflectivity at hourly intervals and averaged over the 6 hours of verification period, for the 25 and 45 dBZ thresholds. Both DA experiments consistently outperform HRRRv4, RRFS p2 CNTL, and NODA across all neighborhood radii. GSI-New achieves the minimum skillful threshold at a radius of 57 km for the 45 dBZ threshold, while JEDI-New reaches it at 63 km. Notably, for the 25 dBZ threshold, forecasts from both DA experiments exceed the skillful threshold even at the 3 km radii (i.e., at the native grid resolution), indicating substantial improvements at the convective scales while the NODA forecasts are non-skillful at all radii for the 45 dBZ, and is only skillful at radii larger than 64 km for the 25 dBZ threshold.

The two reference forecasts also fail to reach the skillful threshold at all radii for the 45 dBZ case, though their FSSs are above those of NODA for radii above 21 km and the differences increase with neighborhood radius (Fig. 10b). The reduced difference in FSS between our DA experiments and the reference forecasts at larger radii may be partly due to reflectivity bias. As discussed in Mittermaier and Roberts (2010), models that underpredict high reflectivity can appear more skillful at large spatial scales because FSS emphasizes spatial agreement over intensity accuracy.

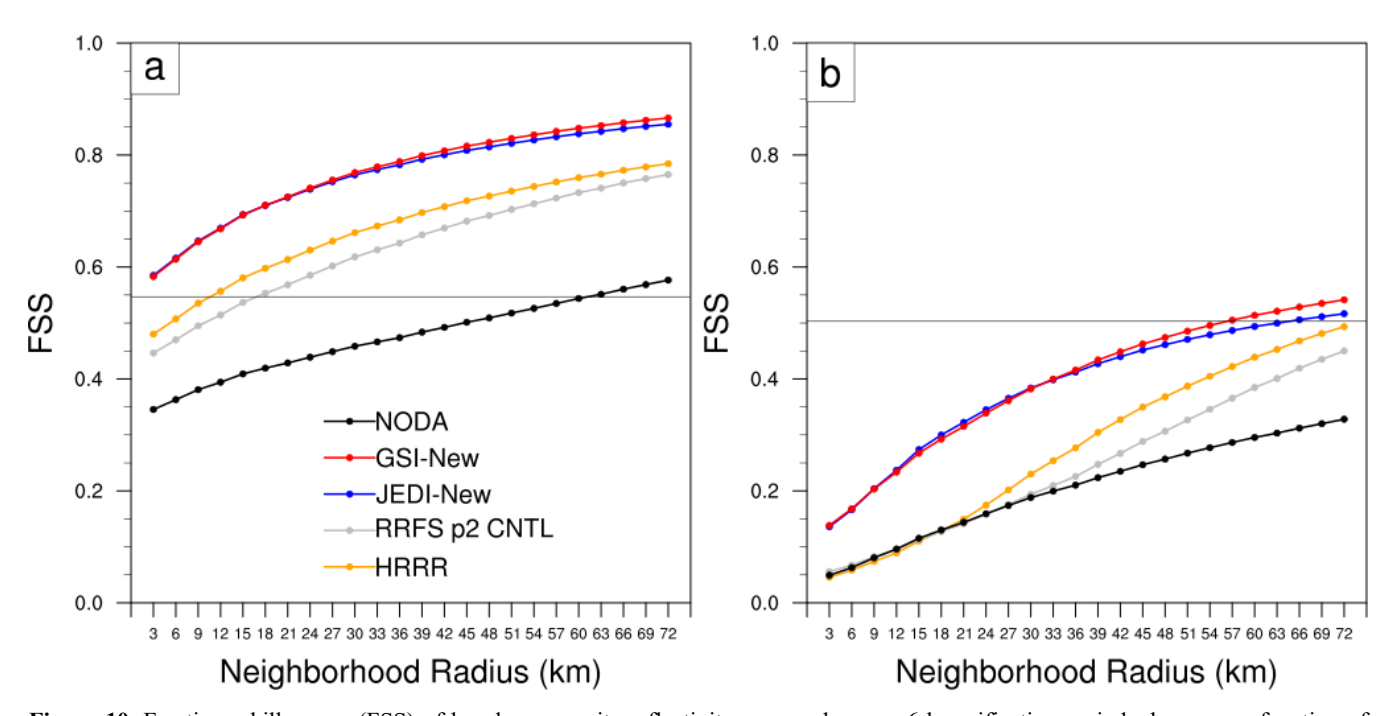


Figure 10. Fractions skill scores (FSS) of hourly composite reflectivity averaged over a 6-h verification period, shown as a function of neighborhood radius (km) for reflectivity thresholds of (a) 25 dBZ and (b) 45 dBZ. Verification is performed against MRMS observations. Results are shown for HRRRv4 (orange), RRFS p2 CNTL (gray), JEDI-New (blue), GSI-New (red), and NODA (black). Thin horizontal line in each panel indicates the minimum skillful forecast threshold.

Figure 11 presents performance diagrams for hourly accumulated precipitation again averaged over the 6 h forecast period, verified against the NCEP Stage IV quantitative precipitation estimates (Lin and Mitchell 2005) at thresholds of 0.04



435

440

445



in. (\approx 1.0 mm) and 0.25 in. (\approx 6.4 mm) against the NCEP Stage IV quantitative precipitation estimates (Lin and Mitchell 2005) at thresholds of 0.04 in. (\approx 1.0 mm) and 0.25 in. (\approx 6.4 mm). At the lower threshold (Fig. 11a), the GSI-New and JEDI-New experiments demonstrate the highest critical success index (CSI), both exceeding 0.6. GSI-New exhibits slightly better skill than JEDI-New, with a CSI above 0.65 and bias close to 1.1. HRRRv4 achieves a CSI of approximately 0.58, while RRFS p2 CNTL and NODA trail behind with CSI values near 0.55 and 0.52, respectively. The DA experiment forecasts demonstrate a favorable combination of detection rate and false alarm control, indicating improved representation of precipitation extent and location compared to other forecasts.

At the higher threshold of 6.35 mm (Fig. 11b), forecast skill decreases for all systems, but the relative ranking remains the same. Both DA experiments maintain CSI values near 0.5, while the reference forecasts drop to around 0.4, and NODA falls below 0.3. The DA experiments also display higher bias (~1.4), suggesting more aggressive precipitation production, consistent with the more active reflectivity fields noted in Fig. 8. In contrast, HRRRv4 exhibits a bias below 1.0 (~0.8), indicating a tendency to underpredict intense precipitation amounts, while RRFS p2 CNTL remains closer to unity. These differences may reflect variations in model configurations and DA approaches; our DA experiments and RRFS p2 CNTL use the FV3-LAM model, which assimilate reflectivity using different approaches while the WRF-based HRRRv4 uses cloud analysis for reflectivity DA and produces weaker precipitation overall. The tendency for FV3-LAM to overpredict precipitation and convective activity has been noted in both cool-season (Supinie et al. 2022) and warm-season ensemble forecasts during the NOAA HWT Spring Forecasting Experiment (Johnson et al. 2025).

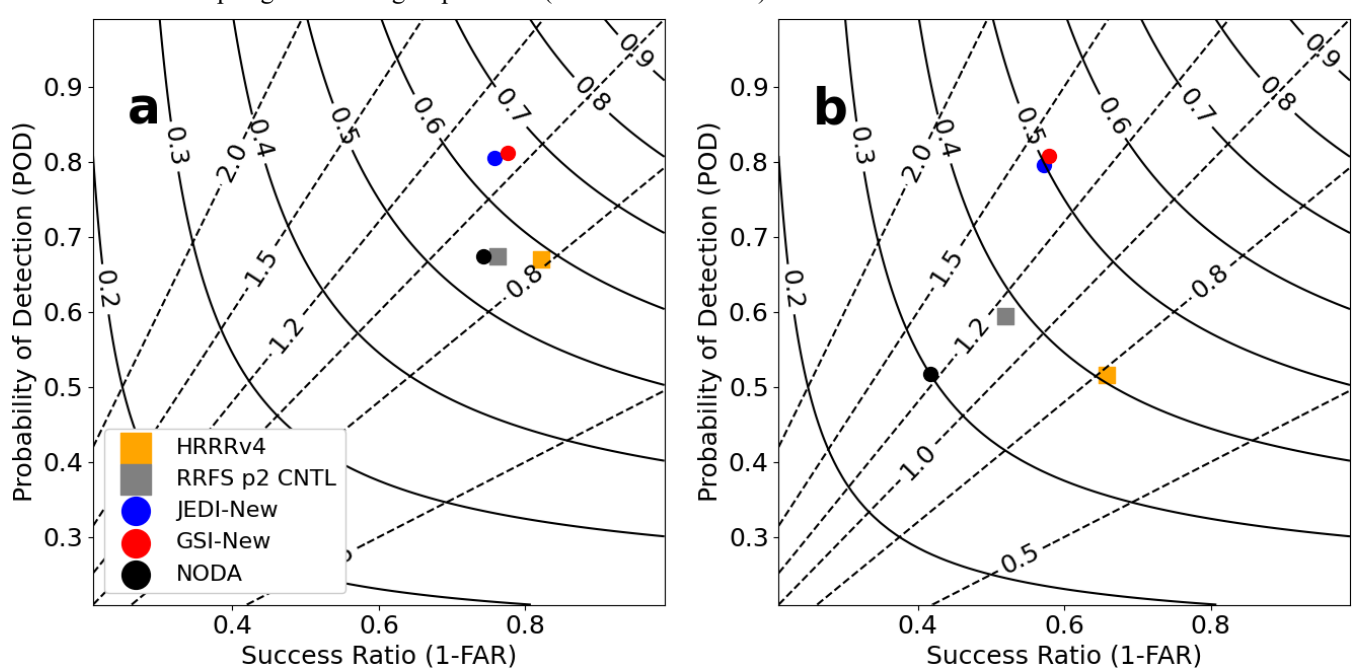


Figure 11. Performance diagrams of hourly accumulated precipitation for a) 1.016 mm and b) 6.35 mm thresholds over the 6-hr forecast period. HRRRv4 (orange square), RRFS p2 CNTL (gray square), JEDI-New (blue circle), GSI-New (red circle), and NODA (black circle) are verified against Stage-IV observation. Black dashed lines and solid contours denote bias and CSI, respectively.



450

455



As described in section 3, our test case involved multiple tornadoes. For convection-allowing predictions, updraft helicity (UH; Kain et al. 2008) is a widely used proxy for diagnosing meso-cyclonic rotation of strong updrafts associated with severe convection, including tornadoes and large hail (Sobash et al. 2011; Gallo et al. 2016). Figure 12 shows the neighborhood probability (NP) of 2-h maximum 2-5 km UH from 0000 to 0200 UTC 13 May 2022 that exceeds 75 m² s⁻², overlaid with Storm Prediction Center reports of tornado, hail, and strong wind. The NP fields are computed using a 42-km neighborhood and subsequently smoothed with an 81-km Gaussian filter (e.g., Tong et al. 2020; Park et al. 2023). Compared to the NODA and reference forecasts, both GSI-New and JEDI-New experiments exhibit substantially higher probabilities and better spatial alignment with the observed severe reports. GSI-New produces a well-defined swath of >80% probabilities extending from northern Iowa to southern Minnesota, coinciding with the location of numerous tornado and wind reports. JEDI-New shows a similar pattern, with a slightly narrower core and minor westward displacement, but still effectively captures the observed event clusters. Both DA experiment forecasts also successfully reproduce the two primary UH clusters associated with the severe convective systems evident in Fig. 2.

The reference forecasts demonstrate weaker performance. HRRRv4 exhibits a reasonably placed UH signal, but with substantially lower probabilities (peak NP ~50%), likely attributable to the use of the WRF model rather than FV3-LAM; the latter is known to produce larger UH values (Potvin et al. 2019). RRFS p2 CNTL generates a broader, westward-shifted UH swath centered over southeastern North Dakota, missing many of the observed reports across Iowa and southern Minnesota. The NODA experiment fails to capture the dominant UH structures altogether, with weak, spatially inconsistent probabilities. These results again demonstrate the positive impacts of directly assimilating radar reflectivity and radial velocity data, using the GSI- and JEDI-based En3DVar, in capturing the location and strength of rotating updrafts associated with severe weather events.





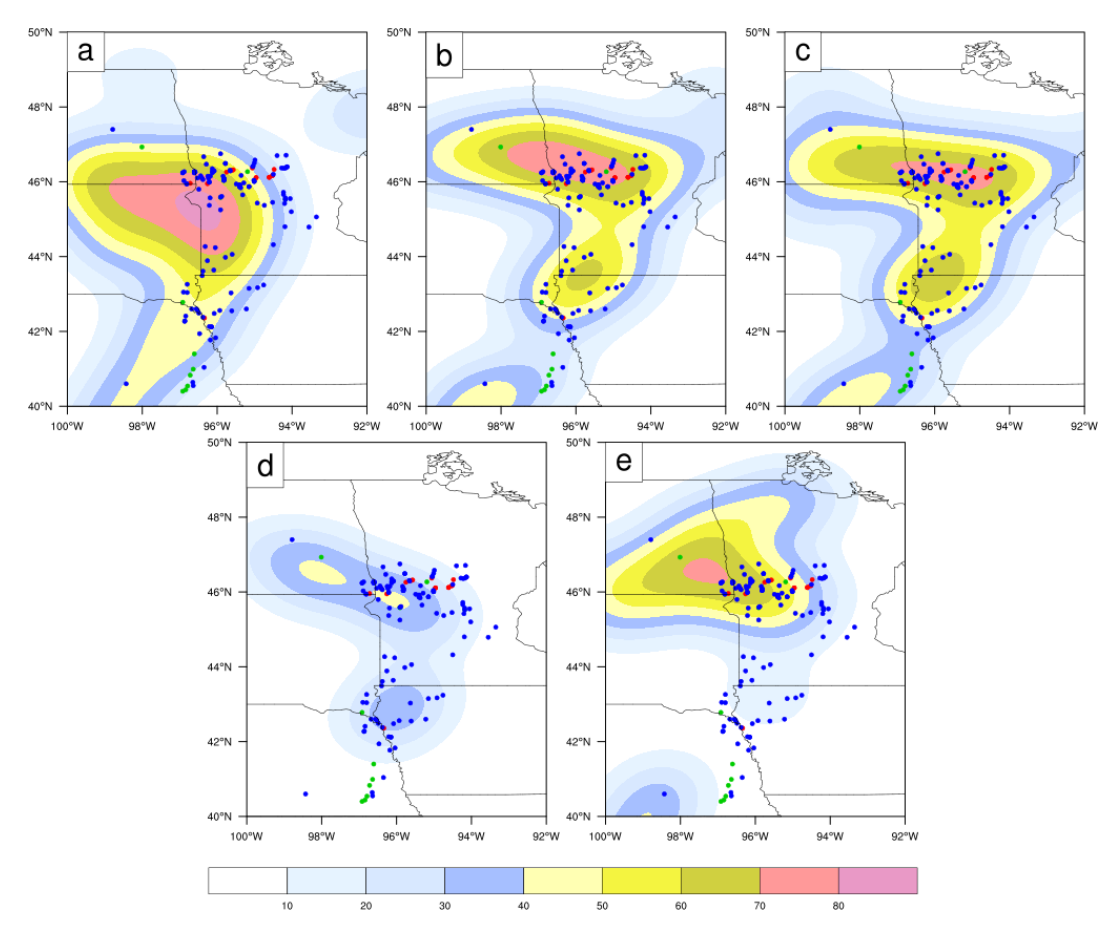


Figure 12. Neighborhood probability (%; shaded) of 2-hr maximum updraft helicity exceeding 75 m2 s-2 from 00 to 02 UTC on May 13, 2022 from the forecasts of a) NODA, b) GSI-New, c) JEDI-New, d) HRRRv4 and e) RRFS p2 CNTL. The red, green, and blue dots are drawn in the plot denote the SPC reports of tornado, hail, and wind, respectively.

5 Summary and conclusions

470

475

480

This study presents the first implementation and evaluation of direct radar reflectivity and radial velocity assimilation within the JEDI En3DVar system, using a microphysics-consistent observation operator for the Thompson double-moment scheme. A high-impact squall-line event that occurred over the Midwest on 13 May 2022 was selected as a test case to assess the performance of the JEDI En3DVar system, using the GSI counterpart and operational forecasts from HRRR and experimental RRFS as references/benchmarks.

The DA experiments assimilated radar observations over a 5-hour window, starting from 1-hour spin-up ensemble forecasts initialized at 1800 UTC and assimilated data at hourly intervals using ensemble covariances generated by parallel ensemble-based DA systems. An updated radar reflectivity operator, consistent with the Thompson microphysics scheme, was used to directly assimilate reflectivity observations into both JEDI and GSI En3DVar systems. Compared to an original operator carried over from GSI En3DVar, the updated version significantly reduced root-mean-square innovations and biases



485

490

495

500

505



for reflectivity in both the background forecast and analysis fields. These improvements stemmed from enhanced treatment of snow and graupel contributions, which led to more consistent hydrometeor adjustments during analysis. As demonstrated by Liu et al. (2022), the physical consistency between the operator and forecast model is crucial for reducing spurious analysis increments and improving assimilation stability.

Forecasts initialized from JEDI and GSI En3DVar analyses using the update reflectivity operator captured two primary mesoscale convective systems with comparable skill. Both systems produced more intense cold pools and better-defined surface wind structures by 0000 UTC, which contributed to improved verification scores for reflectivity and precipitation forecasts over the first 6 hours across multiple thresholds. Additionally, the JEDI-based forecasts showed greater spatial alignment between updraft helicity (UH \geq 75 m² s⁻²) and observed severe weather reports during the first two forecast hours. Despite differences in ensemble generation, localization strategy, and minimization procedures between the JEDI and GSI En3DVar systems, their analyses and short-range forecasts were similarly skillful, indicating that JEDI En3DVar is a viable alternative to the more extensively tested GSI En3DVar for radar DA.

When compared against operational forecasts from HRRR and experimental RRFS, which employed cloud analysis and a Z-state-variable En3DVar approaches, respectively, both JEDI and GSI-based experiments demonstrated slightly improved quantitative forecast skill for reflectivity and precipitation. The probabilistic forecasts of UH also aligned more closely with observed severe weather locations, reinforcing the benefit of direct radar DA in convective-scale systems while demonstrating the implementation correctness of the radar DA capabilities in JEDI En3DVar.

Although the present results demonstrate encouraging performance, they are based on a single convective event. As such, the results may not fully represent the performance of the systems under different meteorological conditions or storm types. Additional experiments involving multiple convective events across various synoptic regimes are necessary to further test the robustness and generality of the observed improvements. Limited by available resources, these are left for future investigations.

While the current study is based on the FV3-LAM model, it should be pointed out that NOAA has initiated a transition to use the Model for Prediction Across Scales (MPAS) dynamic core instead for RRFS version 2 (Alexander et al. 2023). As a result, similar testing and evaluations should be performed that couple JEDI DA with the MPAS forecast system, and these are again left for the future when resources are available.

Code and data availability. The JEDI-FV3 bundle (version 1.0.0) is publicly available from GitHub (https://github.com/JCSDA; JCSDA, 2025) and permanently archived at the Open Science Framework (https://doi.org/10.17605/OSF.IO/PSAEM; Park et al., 2025). The UFS SRW App (public-v2.0.0), which is used for the model simulations, is available from GitHub (https://github.com/ufs-community/ufs-srweather-app; UFS Community, 2022). The MRMS composite reflectivity data (Smith et al., 2016) and NEXRAD Level II radial velocity data (NOAA NCEI, 2022) are publicly accessible from https://mrms.nssl.noaa.gov/ and https://www.ncei.noaa.gov/products/radar/next-generation-weather-



520

530



radar, respectively. For reproducibility, the OSF archive also includes processed radar observations in netCDF format and YAML configuration files for the JEDI EnVar experiments (Park et al., 2025).

Author contributions. JP developed the data assimilation codes, conducted the experiments, performed the diagnostics and plotting, and led the manuscript writing. CL designed the overall study and experiments, analyzed the results, and contributed to the writing. MX contributed to the interpretation of the results and manuscript revision.

Competing interests. The contact author has declared that none of the authors has any competing interests.

Acknowledgments. The authors acknowledge the Texas Advanced Computing Center (TACC) at the University of Texas at 525 Austin for providing high-performance computing resources on the Stampede2 supercomputer through the NSF XSEDE and ACCESS programs. The NEXRAD Level-II data were obtained from the NOAA Next Generation Radar (NEXRAD) public dataset hosted on Google Cloud (https://cloud.google.com/storage/docs/public-datasets/nexrad). The MRMS mosaic data and the GEFS analyses and forecasts were accessed from the NOAA open data repositories on Amazon S3 (https://registry.opendata.aws/noaa-mrms-pds/ and https://registry.opendata.aws/noaa-gefs/).

Financial support. This research has been supported by the National Oceanic and Atmospheric Administration (NOAA) through the Joint Technology Transfer Initiative (JTTI) program (grant no. NA21OAR4590171) and the Research-to-Operations (R2O) program (grant no. NA21OAR4320204).

References

- Alexander, C. R., Carley, J. R., and Pyle, M. E.: The Rapid Refresh Forecast System: Looking Beyond the First Operational Version, in: *Unified Forecast System Implementations and Future Capabilities Workshop (UIFCW 2023)*, Boulder, CO, USA, 25 July 2023, available at: https://epic.noaa.gov/wp-content/uploads/2023/08/UIFCW-2023-Tue-9-Alexander UFS UIFCW 2023 Final-2.pdf (last access: 10 November 2025), 2023.
- Banos, I. H., Mayfield, W. D., Ge, G. Q., Sapucci, L. F., Carley, J. R., and Nance, L.: Assessment of the data assimilation framework for the Rapid Refresh Forecast System v0.1 and impacts on forecasts of a convective storm case study, *Geosci. Model Dev.*, 15, 6891–6917, https://doi.org/10.5194/gmd-15-6891-2022, 2022.
 - Bernardet, L., Bengtsson, L., Reinecke, P. A., Yang, F., Zhang, M., Hall, K., Doyle, J., Martini, M., Firl, G., and Xue, L.: Common Community Physics Package: Fostering collaborative development in physical parameterizations and suites, *Bull. Am. Meteorol. Soc.*, 105, E1490–E1505, https://doi.org/10.1175/BAMS-D-23-0227.1, 2024.



550

560



- Bishop, C. H., Whitaker, J. S., and Lei, L.: Gain form of the ensemble transform Kalman filter and its relevance to satellite data assimilation with model space ensemble covariance localization, *Mon. Weather Rev.*, 145, 4575–4592, https://doi.org/10.1175/MWR-D-17-0102.1, 2017.
 - Brewster, K., Hu, M., Xue, M., and Gao, J.: Efficient assimilation of radar data at high resolution for short-range numerical weather prediction, in: *World Weather Research Programme Symposium on Nowcasting and Very Short-Range Forecasting (WSN05)*, Toulouse, France, WMO, 2005.
 - Chen, L., Liu, C, Xue, M., Zhao, G., Kong, R., and Jung, Y.: Use of power transform mixing ratios as hydrometeor control variables for direct assimilation of radar reflectivity in GSI En3DVar and tests with five convective storm cases, *Mon. Weather Rev.*, 149, 645–659, https://doi.org/10.1175/MWR-D-20-0149.1, 2021.
- Dawson, D. T., Xue, M., Milbrandt, J. A., and Yau, M. K.: Comparison of evaporation and cold pool development between single-moment and multimoment bulk microphysics schemes in idealized simulations of tornadic thunderstorms, *Mon. Weather Rev.*, 138, 1152–1171, https://doi.org/10.1175/2009MWR2956.1, 2010.
 - Dowell, D. C., Alexander, C. R., James, E. P., Weygandt, S. S., Benjamin, S. G., Manikin, G. S., Blake, B. T., Brown, J. M., Olson, J. B., Hu, M., Smirnova, T. G., Ladwig, T., Kenyon, J. S., Ahmadov, R., Turner, D. D., Duda, J. D., and Alcott, T. I.: The High-Resolution Rapid Refresh (HRRR): An hourly updating convection-allowing forecast model. Part I: Motivation and system description, *Wea. Forecasting*, 37, 1371–1395, https://doi.org/10.1175/WAF-D-21-0151.1, 2022.
 - Gallo, B. T., Clark, A. J., and Dembek, S. R.: Forecasting tornadoes using convection-permitting ensembles, *Wea. Forecasting*, 31, 273–295, https://doi.org/10.1175/WAF-D-15-0134.1, 2016.
 - Gao, J., Heinselman, P. L., Xue, M., Wicker, L. J., Yussouf, N., Stensrud, D. J., and Droegemeier, K. K.: The numerical prediction of severe convective storms: Advances, challenges, and outlook, in: *Elsevier Reference Collection in Earth Systems and Environmental Sciences*, Elsevier, 1–22, https://doi.org/10.1016/B978-0-323-96026-7.00127-2, 2024.
 - Grim, J. A., Pinto, J. O., and Dowell, D. C.: Assessing RRFS versus HRRR in predicting widespread convective systems over the eastern CONUS, *Wea. Forecasting*, 39, 121–140, https://doi.org/10.1175/WAF-D-23-0112.1, 2024.
 - Hamill, T. M., and Snyder, C.: A hybrid ensemble Kalman filter–3D variational analysis scheme, *Mon. Weather Rev.*, 128, 2905–2919, https://doi.org/10.1175/1520-0493(2000)128<2905:AHEKFV>2.0.CO;2, 2000.
- Houtekamer, P. L., and Zhang, F.: Review of the ensemble Kalman filter for atmospheric data assimilation, *Mon. Weather Rev.*, 144, 4489–4532, https://doi.org/10.1175/MWR-D-15-0440.1, 2016.
 - Hu, M., Benjamin, S. G., Ladwig, T. T., Dowell, D. C., Weygandt, S. S., Alexander, C. R., and Whitaker, J. S.: GSI three-dimensional ensemble–variational hybrid data assimilation using a global ensemble for the regional Rapid Refresh model, *Mon. Weather Rev.*, 145, 4205–4225, https://doi.org/10.1175/MWR-D-16-0418.1, 2017.
- Hunt, B. R., Kostelich, E. J., and Szunyogh, I.: Efficient data assimilation for spatiotemporal chaos: A local ensemble transform Kalman filter, *Physica D*, 230, 112–126, https://doi.org/10.1016/j.physd.2006.11.008, 2007.



585



- Iacono, M. J., Delamere, J. S., Mlawer, E. J., Shephard, M. W., Clough, S. A., and Collins, W. D.: Radiative forcing by long-lived greenhouse gases: Calculations with the AER radiative transfer models, *J. Geophys. Res. Atmos.*, 113, D13103, https://doi.org/10.1029/2008JD009944, 2008.
- 580 JCSDA: JEDI-FV3 bundle (version 1.0.0), GitHub repository, https://github.com/JCSDA, 2025.
 - Johnson, M., Snook, N., Park, J., Xue, M., Brewster, K. A., Supinie, T., and Hu, X.: Severe weather verification of an FV3-LAM regional ensemble during the 2022 NOAA Hazardous Weather Testbed Spring Forecasting Experiment, *Wea. Forecasting*, 40, 577–592, https://doi.org/10.1175/WAF-D-24-0034.1, 2025.
 - Kain, J. S., et al.: Some practical considerations regarding horizontal resolution in the first generation of operational convection-allowing NWP, *Wea. Forecasting*, 23, 931–952, https://doi.org/10.1175/WAF2007106.1, 2008.
 - Kalina, E. A., Jankov, I., Alcott, T., Olson, J., Beck, J., Berner, J., Dowell, D., and Alexander, C.: A progress report on the development of the High-Resolution Rapid Refresh Ensemble, *Wea. Forecasting*, 36, 791–804, https://doi.org/10.1175/WAF-D-20-0098.1, 2021.
 - Kleist, D. T., Parrish, D. F., Derber, J. C., Treadon, R., Wu, W.-S., and Lord, S.: Introduction of the GSI into the NCEP Global Data Assimilation System, *Wea. Forecasting*, 24, 1691–1705, https://doi.org/10.1175/2009WAF2222201.1, 2009.
 - Kong, R., Xue, M., and Liu, C.: Development of a hybrid En3DVar data assimilation system and comparisons with 3DVar and EnKF for radar data assimilation with observing system simulation experiments, *Mon. Weather Rev.*, 146, 175–198, https://doi.org/10.1175/MWR-D-17-0164.1, 2018.
- Labriola, J., Jung, Y., Liu, C., and Xue, M.: Evaluating forecast performance and sensitivity to the GSI EnKF data assimilation configuration for the 28–29 May 2017 mesoscale convective system case, *Wea. Forecasting*, 36, 127–146, https://doi.org/10.1175/WAF-D-20-0071.1, 2021.
 - Li, H., Liu, C., Xue, M., Park, J., Chen, L., Jung, Y., Kong, R., and Tong, C.-C.: Use of power-transform total number concentration as control variable for direct assimilation of radar reflectivity in GSI En3DVar and tests with six convective storms cases, *Mon. Weather Rev.*, 150, 821–842, https://doi.org/10.1175/MWR-D-21-0041.1, 2022.
- 600 Lin, S.-J.: A "vertically Lagrangian" finite-volume dynamical core for global models, *Mon. Weather Rev.*, 132, 2293–2307, https://doi.org/10.1175/1520-0493(2004)132<2293:AVLFDC>2.0.CO;2, 2004.
 - Lin, Y., and Mitchell, K. E.: The NCEP Stage II/IV hourly precipitation analyses: Development and applications, in: *19th Conf. on Hydrology*, San Diego, CA, Amer. Meteor. Soc., 1.2, available at: https://ams.confex.com/ams/Annual2005/techprogram/paper_83847.htm (last access: 25 September 2025), 2005.
- 605 Liu, C., Xue, M., and Kong, R.: Direct assimilation of radar reflectivity data using 3DVAR: Treatment of hydrometeor background errors and OSSE tests, *Mon. Weather Rev.*, 147, 17–29, https://doi.org/10.1175/MWR-D-18-0033.1, 2019.
 - Liu, C., Xue, M., and Kong, R.: Direct variational assimilation of radar reflectivity and radial velocity data: Issues with nonlinear reflectivity operator and solutions, *Mon. Weather Rev.*, 148, 1483–1502, https://doi.org/10.1175/MWR-D-19-0149.1, 2020.



625

630

635



- 610 Liu, C., Li, H., Xue, M., Jung, Y., Park, J., Chen, L., Kong, R., and Tong, C.: Use of a reflectivity operator based on double-moment Thompson microphysics for direct assimilation of radar reflectivity in GSI-based hybrid En3DVar, *Mon. Weather Rev.*, 150, 907–926, https://doi.org/10.1175/MWR-D-21-0040.1, 2022.
 - Lorenc, A. C.: The potential of the ensemble Kalman filter for NWP a comparison with 4D-Var, *Q. J. Roy. Meteor. Soc.*, 129, 3183–3204, https://doi.org/10.1256/qj.02.132, 2003.
- 615 Ménétrier, B.: Normalized Interpolated Convolution from an Adaptive Subgrid (NICAS) documentation, available at: https://github.com/benjaminmenetrier/nicas-doc (last access: 25 September 2025), 2020.
 - Mittermaier, M., and Roberts, N.: Intercomparison of spatial forecast verification methods: Identifying skillful spatial scales using the Fractions Skill Score, *Wea. Forecasting*, 25, 343–354, https://doi.org/10.1175/2009WAF2222260.1, 2010.
- Niu, G.-Y., et al.: The community Noah land surface model with multiparameterization options (Noah-MP): 1. Model description and evaluation with local-scale measurements, *J. Geophys. Res. Atmos.*, 116, D12109, https://doi.org/10.1029/2010JD015139, 2011.
 - NOAA: 2022 Spring Forecasting Experiment, Hazardous Weather Testbed, National Severe Storms Laboratory, https://doi.org/10.25923/r70a-aw71, 2022.
 - NOAA National Centers for Environmental Information (NCEI): Next Generation Weather Radar (NEXRAD) Level II data, https://www.ncei.noaa.gov/products/radar/next-generation-weather-radar, 2022.
 - NOAA/NCEP Environmental Modeling Center: V2.7 RTMA/URMA/RTMA-RU NCEP OD Science Brief, available at: https://www.emc.ncep.noaa.gov/emc/docs/OD Science Brief RTMA v2.7.pdf (last access: 25 September 2025), 2018.
 - Olson, J. B., Kenyon, J. S., Angevine, W., Brown, J. M., Pagowski, M., and Sušelj, K.: A description of the MYNN-EDMF scheme and the coupling to other components in WRF–ARW, NOAA Office of Oceanic and Atmospheric Research, available at: https://repository.library.noaa.gov/view/noaa/19837 (last access: 25 September 2025), 2019.
 - Park, J., Xue, M., and Liu, C.: Implementation and testing of radar data assimilation capabilities within the Joint Effort for Data assimilation Integration (JEDI) framework with ensemble transformation Kalman filter coupled with FV3-LAM model, *Geophys. Res. Lett.*, 50, e2022GL102709, https://doi.org/10.1029/2022GL102709, 2023.
 - Park, J., Liu, C., and Xue, M.: Processed radar data and YAML configuration files for JEDI EnVar experiments, Open Science Framework, https://doi.org/10.17605/OSF.IO/PSAEM, 2025.
 - Potvin, C. K., et al.: Systematic comparison of convection-allowing models during the 2017 NOAA HWT Spring Forecasting Experiment, *Wea. Forecasting*, 34, 1395–1416, https://doi.org/10.1175/WAF-D-19-0056.1, 2019.
 - Purser, R. J., Wu, W.-S., Parrish, D. F., and Roberts, N. M.: Numerical aspects of the application of recursive filters to variational statistical analysis. Part I: Spatially homogeneous and isotropic Gaussian covariances, *Mon. Weather Rev.*, 131, 1524–1535, https://doi.org/10.1175//2543.1, 2003.
 - Roberts, N. M., and Lean, H. W.: Scale-selective verification of rainfall accumulations from high-resolution forecasts of convective events, *Mon. Weather Rev.*, 136, 78–97, https://doi.org/10.1175/2007MWR2123.1, 2008.



645

650

665



- Schenkman, A. D., Xue, M., Shapiro, A., Brewster, K., and Gao, J.: Impact of CASA Radar and Oklahoma Mesonet data assimilation on the analysis and prediction of tornadic mesovortices in an MCS, *Mon. Weather Rev.*, 139, 3422–3445, https://doi.org/10.1175/MWR-D-10-05051.1, 2011.
- Smith, T. M., et al.: Multi-Radar Multi-Sensor (MRMS) severe weather and aviation products: Initial operating capabilities, *Bull. Am. Meteorol. Soc.*, 97, 1617–1630, https://doi.org/10.1175/BAMS-D-14-00173.1, 2016.
- Snook, N., Xue, M., and Jung, J.: Ensemble probabilistic forecasts of a tornadic mesoscale convective system from ensemble Kalman filter analyses using WSR-88D and CASA radar data, *Mon. Weather Rev.*, 140, 2126–2146, https://doi.org/10.1175/MWR-D-11-00117.1, 2012.
- Sobash, R. A., Kain, J. S., Bright, D. R., Dean, A. R., Coniglio, M. C., and Weiss, S. J.: Probabilistic forecast guidance for severe thunderstorms based on the identification of extreme phenomena in convection-allowing model forecasts, *Wea. Forecasting*, 26, 714–728, https://doi.org/10.1175/WAF-D-10-05046.1, 2011.
- Sun, J., and Crook, N. A.: Dynamical and microphysical retrieval from Doppler radar observations using a cloud model and its adjoint. Part I: Model development and simulated data experiments, *J. Atmos. Sci.*, 54, 1642–1661, https://doi.org/10.1175/1520-0469(1997)054<1642:DAMRFD>2.0.CO;2, 1997.
 - Sun, J., Xue, M., Wilson, J. W., Zawadzki, I., Onvlee-Hooimeyer, J., Ballard, S. P., Joe, P., Barker, D., Lee, P.-H., Golding, B., Xu, M., and Pinto, J.: Use of NWP for nowcasting precipitation: Recent progress and challenges, *Bull. Am. Meteorol. Soc.*, 95, 409–426, https://doi.org/10.1175/BAMS-D-11-00263.1, 2014.
- Supinie, T. A., Park, J., Snook, N., Hu, X., Brewster, K. A., and Xue, M.: Cool-season evaluation of FV3-LAM-based CONUS-scale forecasts with physics configurations of experimental RRFS ensembles, *Mon. Weather Rev.*, 150, 2379–2398, https://doi.org/10.1175/MWR-D-21-0331.1, 2022.
 - Thompson, G., Field, P. R., Rasmussen, R. M., and Hall, W. D.: Explicit forecasts of winter precipitation using an improved bulk microphysics scheme. Part II: Implementation of a new snow parameterization, *Mon. Weather Rev.*, 136, 5095–5115, https://doi.org/10.1175/2008MWR2387.1, 2008.
 - Trémolet, Y., and Auligné, T.: The Joint Effort for Data Assimilation Integration (JEDI), *JCSDA Quarterly Newsletter*, 66, 1–5, https://doi.org/10.25923/RB19-0Q26, 2020.
 - Tong, C.-C., Jung, Y., Xue, M., and Liu, C.: Direct assimilation of radar data within the National Weather Service operational GSI EnKF and hybrid En3DVar systems for the stand-alone regional FV3 model at a convection-allowing resolution, *Geophys. Res. Lett.*, 47, e2020GL090179, https://doi.org/10.1029/2020GL090179, 2020.
 - UFS Community: UFS Short-Range Weather Application (SRW App), GitHub repository, https://github.com/ufs-community/ufs-srweather-app, 2022.
 - Whitaker, J. S., and Hamill, T. M.: Ensemble data assimilation without perturbed observations, *Mon. Weather Rev.*, 130, 1913–1924, https://doi.org/10.1175/1520-0493(2002)130<1913:EDAWPO>2.0.CO;2, 2002.
- Whitaker, J. S., and Hamill, T. M.: Evaluating methods to account for system errors in ensemble data assimilation, *Mon. Weather Rev.*, 140, 3078–3089, https://doi.org/10.1175/MWR-D-11-00276.1, 2012.





Wu, W.-S., Parrish, D. F., Rogers, E., and Lin, Y.: Regional ensemble–variational data assimilation using global ensemble forecasts, *Wea. Forecasting*, 32, 83–96, https://doi.org/10.1175/WAF-D-16-0045.1, 2017.

Zhou, X., et al.: The development of the NCEP Global Ensemble Forecast System version 12, *Wea. Forecasting*, 37, 1069–1084, https://doi.org/10.1175/WAF-D-21-0112.1, 2022.